



Stiffness of the interface between a colloidal body-centered cubic crystal and its liquid

Hyerim Hwang^a, David A. Weitz^{a,b}, and Frans Spaepen^{a,1}

^aSchool of Engineering and Applied Sciences, Harvard University, Cambridge, MA 02138; and ^bDepartment of Physics, Harvard University, Cambridge, MA 02138

Edited by Monica Olvera de la Cruz, Northwestern University, Evanston, IL, and approved August 23, 2020 (received for review March 26, 2020)

Equilibrium interfaces were established between body-centered cubic (BCC) crystals and their liquid using charged colloidal particles in an electric bottle. By measuring a time series of interfacial positions and computing the average power spectrum, their interfacial stiffness was determined according to the capillary fluctuation method. For the (100) and the (114) interfaces, the stiffnesses were 0.15 and 0.18 $k_B T / \sigma^2$ (σ : particle diameter), respectively, and were isotropic in the plane of the interface. For comparison, similar charged colloids were used to create an interface between a face-centered cubic (FCC) crystal and its liquid. Its stiffness was significantly larger: 0.26 $k_B T / \sigma^2$. This result gives experimental support to the explanations offered for the preferential nucleation of BCC over FCC in metallic alloys.

kinetics | crystallization | melting | colloids | interfaces

The body-centered cubic (BCC) phase is found in many metals and alloys, often as the highest-temperature phase, prior to melting. Remarkably, during the solidification of some alloys at undercooled temperatures where the face-centered cubic (FCC) phase is the stable one, it is the metastable BCC phase that preferentially nucleates (1–4). Since the driving force for the nucleation of FCC is then greater than for BCC, the crystal–liquid interfacial energy, γ , for BCC must be smaller than for FCC. To compare interfacial energies, it is useful to normalize them, following Turnbull (5), by the heat of fusion per atom in the interface or $\alpha = \gamma / (\Delta H_f \rho^{2/3})$, where ΔH_f is the enthalpy of fusion per atom and ρ is the atomic number density in the crystal. Analyses of solidification experiments and some structural modeling (4, 6) indicate that α is indeed smaller for BCC than for FCC.

Direct measurements of γ , however, are difficult, but if a dynamic interface can be observed, a related quantity, the interfacial stiffness $\tilde{\gamma}$, can be determined from a time series of measurements of the positional fluctuations of the interface along its normal, $h(y, z, t)$, where y and z are the coordinates in the average interface plane. Fourier transformation of these displacements yields a power spectrum, which upon time averaging, gives according to the capillary fluctuation model (CFM) (7, 8)

$$\langle |A(\mathbf{k})|^2 \rangle = \frac{k_B T}{\tilde{\gamma} k^2}, \quad [1]$$

where \mathbf{k} is a vector parallel to the interface and $\tilde{\gamma} = \gamma + \partial^2 \gamma(\theta) / \partial \theta^2$ is the interface stiffness; θ is the angular variation of the interface normal in the direction of \mathbf{k} , which due to crystal anisotropy, causes a variation in the interface energy, $\gamma(\theta)$. This method has been applied to numerically simulated interfaces (8–12) but experimentally so far only to colloidal FCC–liquid interfaces (13–15).

Results

In this paper, we apply it to a colloidal BCC–liquid system. This is achieved by charging the particles and observing them in an “electric bottle” (16–18). In this device, dielectrophoresis creates a density gradient, which at a specific position, produces a sharp, vertical planar equilibrium interface between a BCC crystal and its liquid. We obtain values for two orientations of the interface

and compare them with the results of numerical simulations of BCC–liquid interfaces using a screened Yukawa potential (19). By changing the charge and screening length of the particles, it is possible to create an FCC–liquid interface as well, the stiffness of which is found to be higher than that of the BCC–liquid interface.

The electric bottle is schematically depicted in Fig. 1A, with details in *Materials and Methods*. Its design differs slightly from that of the cell we used in earlier work on crystallization kinetics (18): both the top and bottom slides have 1-mm-wide Cr/Au electrodes alternated with electrode-free regions. An alternating voltage of 80 V is applied across the electrodes at a frequency of 1 MHz. The electric field profile in the midplane of the two slides, calculated with COMSOL Multiphysics software, is plotted in Fig. 1B. The particles and the suspending medium have dielectric constants ϵ_p and ϵ_m , respectively, in the electric field. The particles acquire an induced dipole moment \vec{p} . Dielectrophoretic forces appear when an electric field gradient ∇E exerts a force $F_{DEP} = (\vec{p} \cdot \nabla) \vec{E} = -V_p \epsilon_{eff} \epsilon_0 \nabla E^2 / 2$ on the induced dipole moment, where $\epsilon_{eff} = 3\beta \epsilon_m / (1 - \beta \phi)^2$ with $\beta = (\epsilon_p - \epsilon_m) / (\epsilon_p + 2\epsilon_m)$, and ϕ and V_p are the volume fraction and volume of the particles, respectively. As the electric bottle is a sealed system, it reaches equilibrium when dielectric forces are balanced by the osmotic pressure forces caused by the particle concentration gradients, which establishes a uniform chemical potential throughout the system.

The colloidal suspension consists of charged poly(methyl methacrylate) (PMMA) particles with diameter $\sigma = 1.8 \mu\text{m}$ that are electrosterically stabilized with poly(hydroxystearic acid) brushes and a solvent mixture of 60 vol/vol % decahydronaphthalene (*cis*-decalin) and 40 vol/vol % tetrachloroethylene. This solvent mixture closely matches both the refractive index of the particles to minimize scattering in confocal microscopy and their density to avoid creaming or sedimentation. Here,

Significance

This paper reports the experimental determination of the stiffness of the interface between a body-centered cubic crystal and its liquid using colloids controlled by dielectrophoresis in an electric bottle. That the measured value is lower than that of alternative interfaces supports the phenomenological explanation invoked for a long-standing observation in phase transformations: the preferential nucleation of body-centered cubic crystals in the solidification of metal alloys.

Author contributions: F.S. designed research; H.H. performed research; H.H. and F.S. analyzed data; and H.H., D.A.W., and F.S. wrote the paper.

The authors declare no competing interest.

This article is a PNAS Direct Submission.

Published under the PNAS license.

¹To whom correspondence may be addressed. Email: spaepen@seas.harvard.edu.

This article contains supporting information online at <https://www.pnas.org/lookup/suppl/doi:10.1073/pnas.2005664117/-DCSupplemental>.

First published September 24, 2020.

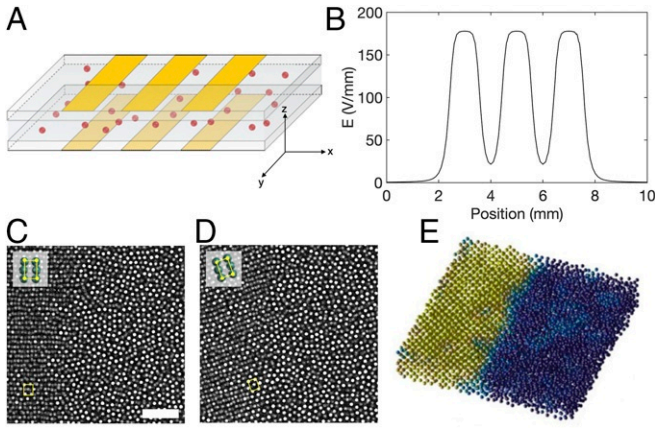


Fig. 1. (A) Schematic figure of the electric bottle. (B) Calculated electric field profile at 80 V. (C and D) Confocal xy images of interfaces between liquid and BCC crystal. The yz interfaces have orientations (C) (100) and (D) (114). (Scale bar: 20 μm .) (E) Reconstructed images of crystal (yellow) and liquid (blue) particles. Projections of the particle positions in the crystals are found in *SI Appendix, Fig. S4*.

the PMMA particles have higher polarizability ($\epsilon_p = 2.6$) than the suspending medium ($\epsilon_m = 2.3$); they move toward stronger electric fields.

Repulsive interactions between particles are established by adding dioctyl sodium sulfosuccinate (AOT). The AOT surfactant molecules, which form inverse micelles above a critical micelle concentration (cmc), charge the particles (20–23). We chose 20 mM concentration to produce a balance between long screening lengths (at low concentration but above the cmc) and high surface charges (at high concentration), at which we anticipate a screening length of $\kappa^{-1} \approx 0.9$ to 1 μm (23); under these conditions, these colloids form crystals at lower volume fractions than hard-sphere colloids. These are known as colloidal Wigner crystals, in analogy to the crystals created by electrons on a semiconductor surface (24).

The particles were located in a confocal microscope (25). The sample cell was equilibrated for 3 d in the microscope room, after which the electric field was applied for 3 d to reach the dielectrophoretic equilibrium. This produced a crystal–liquid interface about 100 μm away from the electrode edge. Each particle in a volume of $100 \times 100 \times 60 \mu\text{m}^3$ was imaged every 15 s. The imaging frequency was chosen to sample a large interface area differently from the earlier measurements on crystallization kinetics, where the image volume needed to be kept sufficiently small to capture the jump frequencies (18). We scanned 200 stacks, consisting of 240 xy slices every 0.25 μm .

Fig. 1 C and D shows two confocal slices of the equilibrated BCC–liquid interfaces. We prepared the suspension with an initial particle volume fraction $\phi \sim 0.1$ (particle number density $\rho = 0.033 \mu\text{m}^{-3}$), less than required for crystallization. We chose this volume fraction based on our empirical observations of the phase behavior (26). The number density of the BCC phase near the interface is $\rho = 0.039 \mu\text{m}^{-3}$. The corresponding conditions of packing fraction and AOT concentration are consistent with the BCC–liquid phase boundary identified by Kanai et al. (21). The crystal always forms with a (110) plane parallel to the coverslip, presumably because this is the crystal plane with the largest areal density and hence, the favored one in heterogeneous crystal nucleation. Two vertical interfaces formed side by side at the same electrode edge, one with a (100) crystal boundary and the other with a (114) boundary.

We define the interface by assigning a structure to each individual particle. An order parameter ψ_i , which we define as the number of in-line neighbor pairs (bond angles of $180 \pm 19^\circ$)

in nearest and next-nearest neighbor particles is used to distinguish the crystal from liquid (27). A perfect BCC crystal has an order parameter 7, four from nearest neighbor pairs and three from next-nearest neighbor pairs. We classify particles with $\psi_i > 3.5$ as crystalline and all others as liquid. A rendering of crystalline and liquid particles is shown in Fig. 1E. In addition, we use the number of crystal bonds Z , which is the number of crystal neighbors of a particle (14, 18). In an ideal BCC crystal, Z is 14. Next, we categorize the crystalline particles ($\psi_i > 3.5$) into two groups: crystal ($Z \geq 13$) and interface ($12 \geq Z \geq 7$). The interface particles lie between the two phases and form a continuous two-dimensional surface with an area of $45 \times 90 \mu\text{m}^2$. In most cases, the interface is close to parallel to the yz plane, indicated in Fig. 1A.

The height variations from the time-averaged position are given by

$$h(y, z, t) = x(y, z, t) - \langle x(y, z) \rangle_t. \quad [2]$$

The Fourier transform is calculated according to

$$A(\mathbf{k}) = h(m, n) = \frac{\Delta_{yz}^2}{\sqrt{S}} \left[\sum_{jk} h(j, k) e^{-i(\frac{2\pi}{L})mj} e^{-i(\frac{2\pi}{L})nk} \right], \quad [3]$$

where S is the total area in real space, L is the number of grid points, and $\Delta_{yz} = 0.5 \mu\text{m} = 0.28 \sigma$ is the spacing of the grid at which the values of h are interpolated. Edge effects are minimized by imposing a circular mask with diameter equal to the edge length of the interface.

The inverse averaged power spectra $\langle |A(\mathbf{k})|^2 \rangle^{-1}$, obtained from 200 configurations of the (100) and (114) interfaces, are shown as linear contour plots in Fig. 2. They appear to be azimuthally isotropic at low k , which corresponds to the continuum limit of the CFM. The variation of the interfacial stiffness with angle in the plane of the interface is described by a second-rank tensor (28). This implies that the stiffness of a fourfold symmetric (100) interface should be isotropic, as indeed it is. The stiffness of a (114) interface, however, should be anisotropic, which it is not. A similar observation was made in hard-sphere FCC–liquid interfaces, where the (110) interfacial stiffness was found to be isotropic (14, 15). These discrepancies remain unexplained.

The power spectra are angularly averaged to calculate the interfacial stiffness. Fig. 3A is a log–log plot of $\langle |A(\mathbf{k})|^2 \rangle$ vs. k for (100). At low k , the data follow the k^{-2} behavior of the CFM. We chose the range of $0.32 \sigma^{-1} < k < 0.63 \sigma^{-1}$ because a straight-line fit through the points in that range had a slope closest to -2 (-2.03 ± 0.18). Fig. 3B shows the linear fit of $\langle |A(\mathbf{k})|^2 \rangle^{-1}$ vs. k^2 , which according to Eq. 1, gives an interfacial stiffness of $\tilde{\gamma} = 0.149 \pm 0.010 k_B T / \sigma^2$ with an offset $-0.003 \pm 0.003 \sigma^{-4}$. For the (114) interface, the power spectrum of Fig. 3C gives a range

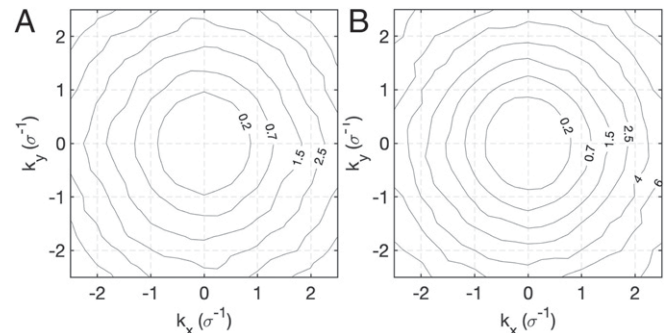


Fig. 2. Linear contour plots of the inverse Fourier power spectrum $\langle |A(\mathbf{k})|^2 \rangle^{-1}$ of the (A) (100) and (B) (114) interfaces planes.

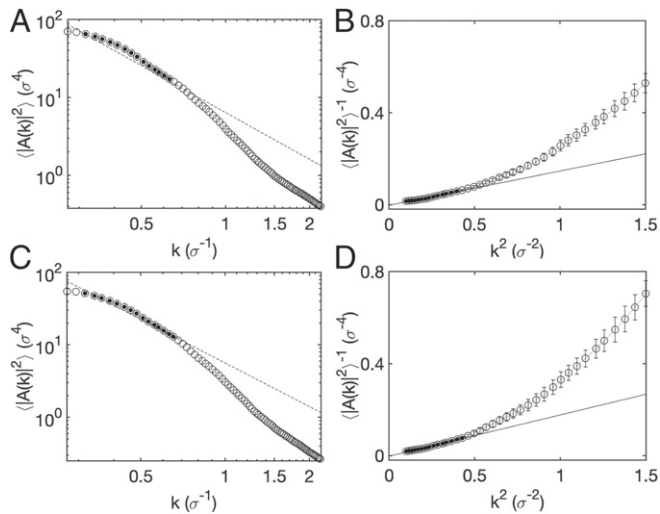


Fig. 3. (A and C) The power spectra $\langle |A(\mathbf{k})|^2 \rangle^{-1}$ vs. k for the (A) (100) and (C) (114) interfaces. The filled dots correspond to a k^{-2} dependence (dashed lines) consistent with CFM. (B and D) Inverse of the angularly averaged power spectra of the (B) (100) and (D) (114) interfacial height profiles as a function of k^2 , with a linear regression to the small wave vector region.

$0.32 \sigma^{-1} < k < 0.65 \sigma^{-1}$ where the CFM applies. The corresponding linear fit in Fig. 3D gives $\tilde{\gamma} = 0.179 \pm 0.011 k_B T / \sigma^2$ with an offset $0.002 \pm 0.003 \sigma^{-4}$. That the offsets in Fig. 3B and D are close to zero is the result of the force that stabilizes the interface position having a negligible differential effect on the two phases. In the earlier colloid experiments (14, 15), this force was provided by gravity, and the interface was horizontal. In the experiments with the heavier silica colloids, there were measurable offsets, which could quantitatively be accounted for by the density difference between the two phases (14). In the later experiments with the more density-matched polymeric particles, the offsets were negligible (15). In the present experiments, gravity plays no role: the interface is vertical, and the displacements are horizontal. The interface is stabilized by the horizontal dielectrophoretic force. As shown in *SI Appendix*, the corresponding offsets caused by the difference in density between the two phases are indeed negligible.

By fitting $\langle |A(\mathbf{k})|^2 \rangle^{-1}$ vs. k^2 , for low values of k , along a range of directions $\hat{\mathbf{k}}$ in the plane of the interface, the angular dependence of the stiffness could be determined. The results are shown in Fig. 4, and they confirm the isotropy observed in Fig. 2. The variation in the values also provides an estimate of the uncertainty in the measurements, which is about 10%.^{*} Note that the apparent angular variation of $\tilde{\gamma}$ of the (114) interface is smaller than that of the isotropic (100) interface and hence, does not signify any anisotropy.

Since it is of interest to compare the properties of the BCC-liquid interfaces with those of the FCC-liquid interface, we created the latter in a similar system of charge-stabilized colloids. The addition of only 5 mM AOT causes weaker repulsion between the particles and produces the FCC phase at high volume fractions. Fig. 5A is a confocal slice of an FCC-liquid interface at equilibrium. The number density of the FCC crystal is $\rho = 0.067 \mu\text{m}^{-3}$, and its volume fraction is $\phi = 0.20$. These values are much lower than those of the hard-sphere colloidal FCC crystal-liquid interface studied in earlier work ($\rho = 0.27$ and $\phi = 0.53$) (14, 15) and closer to those of our

BCC-liquid system. They are also not entirely consistent with the phase diagram of Kanai et al. (21, figure 3 c and f): they do fall in the FCC field, but they are not on the FCC-liquid phase boundary. The orientation of the interfacial plane is (110). As shown in Fig. 5B, its interfacial stiffness is isotropic in the plane, against the expectation from its twofold symmetry but in agreement with the earlier observations on colloidal hard-sphere FCC-liquid interfaces (14, 15). The fit in Fig. 5D for $0.32 \sigma^{-1} < k < 0.80 \sigma^{-1}$, which corresponds to best linear fit (exponent of -2.1 ± 0.1) in Fig. 5C, gives $\tilde{\gamma} = 0.264 \pm 0.015 k_B T / \sigma^2$ with an offset $-0.008 \pm 0.005 \sigma^{-4}$.

The data are summarized in Table 1, together with other colloidal data of colloid experiments and simulation results (15, 19). In units of $k_B T / \sigma^2$, the stiffnesses of the charged colloid BCC interfaces are smaller than that of the charged colloid FCC interface, which in turn, is smaller than those of the hard-sphere FCC interfaces. Part of these differences arises from the very different densities. We therefore compare the dimensionless quantities $\tilde{\gamma} \rho^{-2/3} / k_B T$, which show a similar but less pronounced order. The latter quantity is also reported in the only simulation of the BCC interfacial stiffness for charged colloids, which uses a screened Yukawa potential (19). The simulation values are substantially below the measured ones for reasons that are not immediately clear. Furthermore, unlike the measurements, the simulations found the (110) interface to be anisotropic. A similar discrepancy was found between experiments and simulations of the (110) hard-sphere interfaces (14, 15, 29–31).

Discussion

Since the interfacial properties directly affect the crystal nucleation kinetics, it is useful to compare the values of the stiffnesses with their Turnbull normalization: $\tilde{\alpha} = \frac{\tilde{\gamma} \rho^{-2/3}}{\Delta H_f} = \frac{\tilde{\gamma} \rho^{-2/3}}{\Delta s_f k_B T}$, where Δs_f is the dimensionless entropy of fusion (units of k_B) (5). For the charged colloids, we use the entropies calculated by Robbins et al. (32) (Fig. 5) for Yukawa systems, which depend on the parameter $\lambda = \kappa \rho^{-1/3}$, where κ^{-1} is the screening length. For the BCC phase, the screening length obtained from the AOT concentration is in good agreement[†] with that obtained from the phase diagram: $\kappa^{-1} = 0.91 \mu\text{m}$. This gives an entropy of fusion $\Delta s_f = 0.69$. For the FCC phase, the value is not clear: the AOT concentration gives $\kappa^{-1} = 1.6 \mu\text{m}$, but the phase diagram gives $\kappa^{-1} = 0.81 \mu\text{m}$. For the crystal-liquid phase boundary at the measured packing fraction, the phase diagram gives $\kappa^{-1} = 0.18 \mu\text{m}$. The FCC entropy of fusion therefore may fall in the range $\Delta s_f = 0.54$ to 0.72 . We use the lower value since it has a direct observational basis (i.e., the phase boundary between FCC and the liquid and the packing fraction), whereas the other values may differ because of the subtle shifts in the AOT micelle structure. For the entropy of fusion of the hard-sphere system, we use the value calculated by Alder et al. (33): $\Delta s_f = 1.09$. The resulting values of $\tilde{\alpha}$ are listed in Table 1.

We observe that the values of $\tilde{\alpha}$ for BCC are lower than those for FCC. We note that the higher value of $\tilde{\alpha}$ for charged colloid FCC, which corresponds to the preferred lower value of Δs_f , is close to the $\tilde{\alpha}$ values for the FCC hard-sphere colloid interfaces, consistent with the repulsion of the charged colloids in the FCC phase being short range.

We believe that the normalized interfacial stiffnesses, $\tilde{\alpha}$, are valid proxies for comparing the relative values of the normalized interfacial energies α . The difference between the two quantities arises from the anisotropy of the interfacial energy γ , which

^{*}A detailed discussion of the uncertainty limit is in *SI Appendix*.

[†]See figure 4 in ref. 23 and figure 3 c and f in ref. 21.

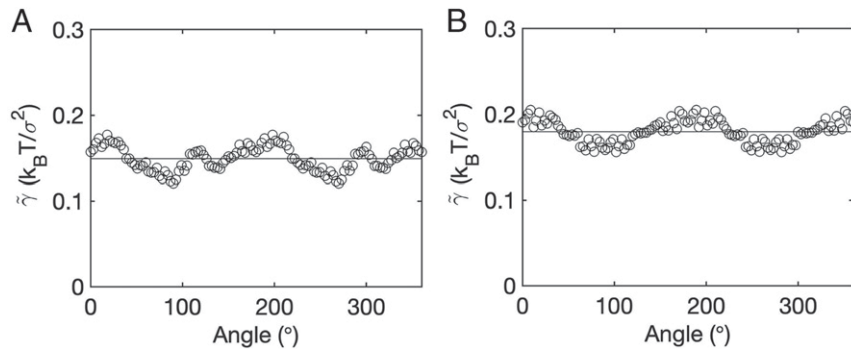


Fig. 4. Interfacial stiffness as a function of in-plane angle for the (A) (100) and (B) (114) interfaces. The horizontal lines indicate the averaged stiffness.

gives rise to the term γ'' in Eq. 1. This means that the values of $\tilde{\gamma}$ at the high-symmetry orientations represent extrema in the angular dependence and that they bracket the value of the only weakly anisotropic γ , as is indeed seen in computer simulations (6). The experiments on the FCC hard-sphere colloids show that the spread of $\tilde{\gamma}$ and hence, $\tilde{\alpha}$ is about 20%, which means that α is about 10% lower than the maximum value of $\tilde{\alpha}$ at (110). Using this result on the preferred value of $\tilde{\alpha}$ for the charged colloid FCC (110) interface gives $\alpha \approx 0.8$. The anisotropy of the BCC–liquid interfacial energy is much weaker than that for FCC, with the spread between the extreme values of $\tilde{\gamma}$ being less than 5%, so that $\tilde{\alpha}$ is close to α (6).

We therefore feel justified, for the purposes of comparison, in using the measured interfacial stiffnesses as proxies for the interfacial energy and that the inequality we have measured between $\tilde{\alpha}$ for BCC and FCC is the most direct experimental evidence to date for the classical nucleation interpretation of the

experiments in which the nucleation of metastable BCC phase is favored.

It would be of interest to apply our results directly to the interpretation of homogeneous crystal nucleation experiments in similar colloidal systems. Tan et al. (34) have performed such experiments and report the presence of hexagonal close packed–like precursor coordinations in the liquid leading to the formation of metastable BCC or FCC phases. To test the classical nucleation interpretation, however, it would be necessary to perform the experiments under conditions that yield sufficiently large critical nuclei with a well-formed crystal–liquid interface.

Materials and Methods

The electric bottle (Fig. 1A) consists of two glass slides ($22 \times 22 \text{ mm}^2$) that are separated by $\sim 200 \mu\text{m}$ and filled with a colloidal suspension. The top and bottom plates have three 1-mm-wide Cr/Au electrodes separated by

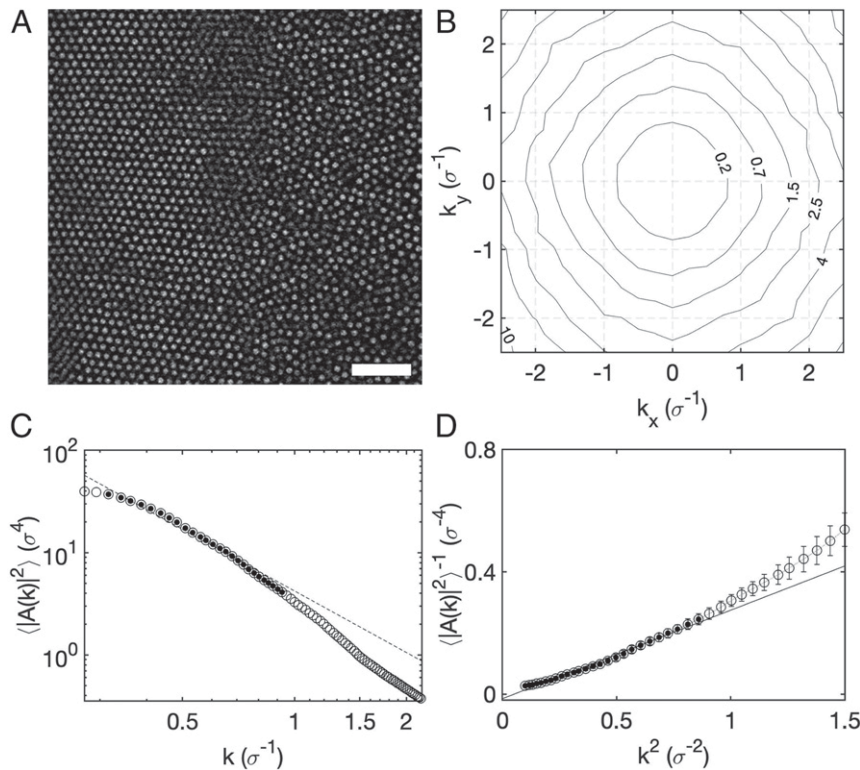


Fig. 5. (A) Confocal xy image of an interface between liquid and FCC crystal, with yz interface orientation (110). (Scale bar: $20 \mu\text{m}$.) (B) Linear contour plot of the inverse Fourier power spectrum. (C) The power spectrum $\langle |A(k)|^2 \rangle^{-1}$ vs. k . (D) Inverse of the angularly averaged power spectrum as a function of k^2 with a linear regression to the small wave vector region.

Table 1. Calculated and measured $\bar{\gamma}$ values of the crystal–liquid interface stiffness, $\bar{\gamma}$; the packing fraction, ϕ ; the particle number density ρ of the crystal; dimensionless stiffness, $\bar{\gamma}\rho^{-2/3}/k_B T$; and the Turnbull parameter, $\bar{\alpha}$ (in the text)

	$\bar{\gamma}$ ($k_B T/\sigma^2$)	ϕ	ρ (μm^{-3})	$\bar{\gamma}\rho^{-2/3}/k_B T$	$\bar{\alpha}$	Sample	Source
BCC (100)	0.15 ± 0.01	0.11	0.039	0.40 ± 0.03	0.58	Charged colloids	This work
BCC (114)	0.18 ± 0.01	0.11	0.039	0.48 ± 0.03	0.68	Charged colloids	This work
FCC (110)	0.26 ± 0.01	0.20	0.067	0.49 ± 0.03	0.67–0.92	Charged colloids	This work
BCC (100)				0.132		Yukawa simulation	Heinonen et al. (19)
BCC (110) _x				0.138		Yukawa simulation	Heinonen et al. (19)
BCC (110) _y				0.120		Yukawa simulation	Heinonen et al. (19)
BCC (111)				0.136		Yukawa simulation	Heinonen et al. (19)
FCC (100)	0.47	0.53	0.27	1.13	1.04	Hard-sphere colloids	van Loenen et al. (15)
FCC (111)	0.41	0.53	0.27	0.98	0.90	Hard-sphere colloids	van Loenen et al. (15)
FCC (110)	0.53	0.53	0.27	1.27	1.17	Hard-sphere colloids	van Loenen et al. (15)

1 mm. We apply an AC voltage of 80 V across the electrodes at a frequency of 1 MHz.

Data Availability. All study data are included in the article and [SI Appendix](#).

ACKNOWLEDGMENTS. We thank Winfield Hill of the Rowland Institute at Harvard for his assistance with the design and construction of the electronics. This work has been supported by NSF Contracts DMR-1206765 and DMR-1611089.

- R. E. Cech, Undercooling of Fe-Ni droplets. *Trans. Metall. AIME* **206**, 585 (1956).
- D. Turnbull, Metastable structures in metallurgy. *Metall. Mater. Trans. B* **12**, 695–708 (1981).
- T. Volkman, D. M. Herlach, W. Löser, Nucleation and phase selection in undercooled Fe-Cr-Ni melts. Part II. Containerless solidification experiments. *Metall. Mater. Trans. A* **28**, 461–469 (1997).
- D. Herlach, D. Holland-Moritz, P. Galenko, *Metastable Solids from Undercooled Melts* (Elsevier, 2006).
- D. Turnbull, Formation of crystal nuclei in liquid metals. *J. Appl. Phys.* **21**, 1022–1028 (1950).
- D. Y. Sun, M. Asta, J. J. Hoyt, Crystal-melt interfacial free energies and mobilities in FCC and BCC Fe. *Phys. Rev. B* **69**, 174103 (2004).
- A. Karma, Fluctuations in solidification. *Phys. Rev. E* **48**, 3441–3458 (1993).
- J. J. Hoyt, M. Asta, A. Karma, Method for computing the anisotropy of the solid-liquid interfacial free energy. *Phys. Rev. Lett.* **86**, 5530 (2001).
- J. J. Hoyt, Atomistic and continuum modeling of dendritic solidification. *Mater. Sci. Eng. R* **41**, 121–163 (2003).
- J. J. Hoyt, M. Asta, Atomistic computation of liquid diffusivity, solid-liquid interfacial free energy, and kinetic coefficient in Au and Ag. *Phys. Rev. B* **206**, 214106 (2002).
- J. R. Morris, Complete mapping of the anisotropic free energy of the crystal-melt interface in Al. *Phys. Rev. B* **66**, 144104 (2002).
- J. R. Morris, X. Song, The anisotropic free energy of the Lennard-Jones crystal-melt interface. *J. Chem. Phys.* **119**, 3920–3925 (2003).
- J. Hernandez-Guzman, E. R. Weeks, The equilibrium intrinsic crystal-liquid interface of colloids. *Proc. Natl. Acad. Sci. U.S.A.* **106**, 15198–15202 (2009).
- I. B. Ramsteiner, D. A. Weitz, F. Spaepen, Stiffness of the crystal-liquid interface in a hard-sphere colloidal system measured from capillary fluctuations. *Phys. Rev. E* **82**, 041603 (2010).
- S. Z. van Loenen et al., Measurement of the stiffness of hard-sphere colloidal crystal-liquid interfaces. *Phys. Rev. Mater.* **3**, 085605 (2019).
- M. T. Sullivan et al., An electric bottle for colloids. *Phys. Rev. Lett.* **96**, 015703 (2006).
- M. E. Leunissen, M. T. Sullivan, P. M. Chaikin, A. Van Blaaderen, Concentrating colloids with electric field gradients. I. Particle transport and growth mechanism of hard-sphere-like crystals in an electric bottle. *J. Chem. Phys.* **128**, 164508 (2008).
- H. Hwang, D. A. Weitz, F. Spaepen, Direct observation of crystallization and melting with colloids. *Proc. Natl. Acad. Sci. U.S.A.* **116**, 1180–1184 (2019).
- V. Heinonen et al., BCC crystal-fluid interfacial free energy in Yukawa systems. *J. Chem. Phys.* **138**, 044705 (2013).
- E. R. Russell, F. Spaepen, D. A. Weitz, Anisotropic elasticity of experimental colloidal Wigner crystals. *Phys. Rev. E* **91**, 032310 (2015).
- T. Kanai et al., Crystallization and reentrant melting of charged colloids in nonpolar solvents. *Phys. Rev. E* **91**, 030301 (2015).
- J. Sprakel, A. Zaccaro, F. Spaepen, P. Schall, D. A. Weitz, Direct observation of entropic stabilization of BCC crystals near melting. *Phys. Rev. Lett.* **118**, 088003 (2017).
- M. F. Hsu, E. R. Dufresne, D. A. Weitz, Charge stabilization in nonpolar solvents. *Langmuir* **21**, 4881–4887 (2005).
- E. Wigner, Effects of the electron interaction on the energy levels of electrons in metals. *Trans. Faraday Soc.* **34**, 678–685 (1938).
- K. E. Jensen, N. Nakamura, An iterative algorithm to improve colloidal particle locating. *Rev. Sci. Instrum.* **87**, 066103 (2016).
- H. Hwang, “Crystal-liquid transitions studied with colloids in an electric bottle,” PhD thesis, Harvard University, Cambridge, MA (2016).
- G. J. Ackland, A. P. Jones, Applications of local crystal structure measures in experiment and simulation. *Phys. Rev. B* **73**, 054104 (2006).
- H. Zhang, D. Du, D. J. Srolovitz, M. I. Mendelev, Determination of grain boundary stiffness from molecular dynamics simulation. *Appl. Phys. Lett.* **88**, 121927 (2006).
- R. L. Davidchack, J. R. Morris, B. B. Laird, The anisotropic hard-sphere crystal-melt interfacial free energy from fluctuations. *J. Chem. Phys.* **125**, 094710 (2006).
- M. Amini, B. B. Laird, Kinetic coefficient for hard-sphere crystal growth from the melt. *Phys. Rev. Lett.* **97**, 216102 (2006).
- Y. Mu, A. Houk, X. Song, Anisotropic interfacial free energies of the hard-sphere crystal-melt interfaces†. *J. Phys. Chem. B* **109**, 6500–6504 (2005).
- M. O. Robbins, K. Kremer, G. S. Grest, Phase diagram and dynamics of Yukawa systems. *J. Chem. Phys.* **88**, 3286–3312 (1988).
- B. J. Alder, W. G. Hoover, D. A. Young, Studies in molecular dynamics. V. High-density equation of state and entropy for hard disks and spheres. *J. Chem. Phys.* **49**, 3688–3696 (1968).
- P. Tan, N. Xu, L. Xu, Visualizing kinetic pathways of homogeneous nucleation in colloidal crystallization. *Nat. Phys.* **10**, 73–79 (2014).